ACS APPLIED MATERIALS & INTERFACES

Research Article

www.acsami.org

Surface Defects on Natural MoS_2

Rafik Addou,*,† Luigi Colombo,‡ and Robert M. Wallace*,†

†Department of Materials Science and Engineering, The University of Texas at Dallas, 800 West Campbell Road, Richardson, Texas 75080, United States

‡Texas Instruments Incorporated, 13121 TI Boulevard, MS-365, Dallas, Texas 75243, United States

S Supporting Information

ABSTRACT: Transition metal dichalcogenides (TMDs) are being considered for a variety of electronic and optoelectronic devices such as beyond complementary metal-oxide-semiconductor (CMOS) switches, light-emitting diodes, solar cells, as well as sensors, among others. Molybdenum disulfide (MoS_2) is the most studied of the TMDs in part because of its availability in the natural or geological form. The performance of most devices is strongly affected by the intrinsic defects in geological MoS_2. Indeed, most sources of current transition metal dichalcogenides have defects, including many impurities. The variability in the electrical properties of MoS_2 across the surface of the same crystal has been shown to be correlated with local variations in stoichiometry as well as metallic-like and structural defects. The presence of impurities has also been suggested to play a role in determining the Fermi level in MoS_2. The main focus of this work is to highlight a number of intrinsic defects detected on natural, exfoliated MoS_2 crystals from two different sources that have been often used in previous reports for device fabrication. We employed room temperature scanning tunneling microscopy (STM) and spectroscopy (STS), inductively coupled plasma mass spectrometry (ICPMS), as well as X-ray photoelectron spectroscopy (XPS) to study the pristine surface of $MoS_2(0001)$ immediately after exfoliation. ICPMS used to measure the concentration of impurity elements can in part explain the local contrast behavior observed in STM images. This work highlights that the high concentration of surface defects and impurity atoms may explain the variability observed in the electrical and physical characteristics of MoS_2.

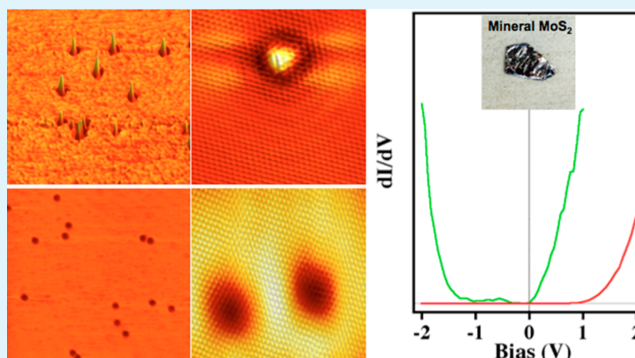

KEYWORDS: *MoS_2, intrinsic defects, vacancy, impurity, intrinsic doping, scanning tunneling microscopy/spectroscopy, inductively coupled plasma mass spectrometry*

INTRODUCTION

After the isolation of graphene, there has been an increased interest in all related two-dimensional (2D) materials (e.g., hexagonal boron nitride, graphane, silicene, transition metal dichalcogenides, etc.)[1] resulting in many studies on both isolated single layers[2−4] and on stacked 2D heterostructures.[5,6] The difficulty of opening a band gap in graphene has limited its integration into current device architectures.[7] In contrast, many transition metal dichalcogenides, such as molybdenite (MoS_2), are semiconductors possessing a natural band gap. For MoS_2, this band gap ranges between 1.2 and 1.8 eV, depending on its thickness,[8,9] making it suitable for diverse applications for nano- and optoelectronics.[7,10] MoS_2 is a layered crystal consisting of two atomic layers of close-packed S atoms separated by one close-packed Mo atomic layer (S−Mo−S).[11,12] Atoms within each layer are strongly bonded by covalent interactions, while the interactions between layers are through weak van der Waals forces enabling easy exfoliation. Ideally, the cleaved surface is expected to yield a dearth of dangling bond states and defects, raising the prospect of a desirable, low defect density device interface.

Accurate control of the entire semiconductor interface prior to (and during) device integration is crucial to achieve maximum device performance and reliability. Numerous scanning tunneling microscopy studies of the basal plane of MoS_2 have contributed to the understanding of the atomic structure of the defect-free surface.[13−17] Besides MoS_2, a number of other layered crystals belonging to the class of transition metal dichalcogenides (TMDs) MX_2 (M = Mo, W, Ta, Re, Nb; X = S, Se, Te) have been successfully imaged, as reported in STM studies of $ReSe_2$,[18] ReS_2,[19] WSe_2,[20,21] $NbTe_2$,[22,23] WTe_2,[23,24] $MoTe_2$,[25,26] $MoSe_2$,[27,28] TaS_2,[29,30] and $TaSe_2$.[29,30] In general STM can be used to image the surface of materials and to also specifically detect imperfections. To correlate these imperfections and defects (vacancy, impurity, adatoms, etc.) with the electronic structure, several theoretical and experimental studies of induced and/or natural defects have been carried out.[17,19,21,28,30−34]

Received: February 26, 2015
Accepted: May 17, 2015
Published: May 17, 2015

ACS Publications © 2015 American Chemical Society

DOI: 10.1021/acsami.5b01778
ACS Appl. Mater. Interfaces 2015, 7, 11921−11929

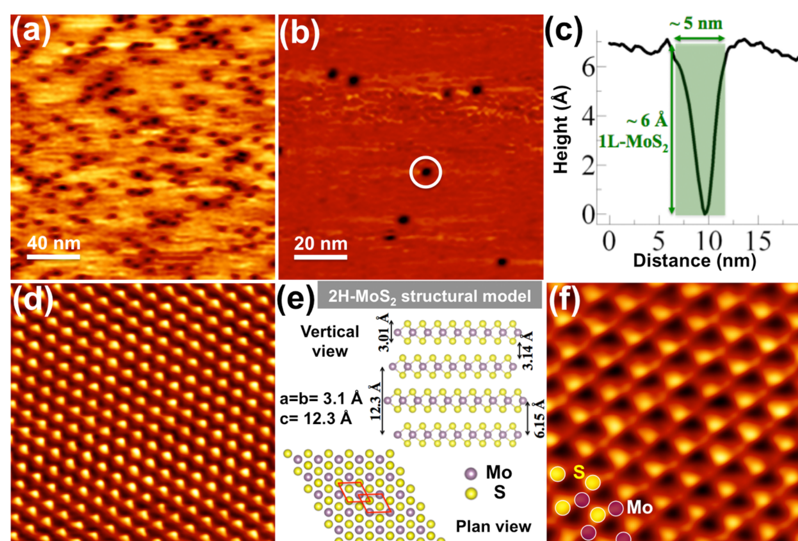

Figure 1. Topography of the "as-exfoliated" MoS_2 crystal from both sources. (a) Large STM image (V_{bias} = +1.5 V, I_t = 0.3 nA) exhibits dark defects with high defect density. (b) STM image (V_{bias} = −300 mV, I_t = 0.5 nA) recorded on low defect density area. (c) Line profile taken across the dark defect outlined in panel b; the green box shows an example of the defect dimensions (5 nm × 0.6 nm). (d) High resolution STM image (5 nm × 5 nm, V_{bias} = +150 mV, I_t = 0.2 nA, R_{gap} = 750 MΩ) shows a hexagonal pattern in defect-free area. (e) Schematic representation of the 2H-MoS_2 bulk structure. The 2H-MX_2 polytype possess trigonal prismatic coordination that has two X−M−X layers per unit cell. (f) Well-resolved STM image (2.5 nm × 2.5 nm, V_{bias}=+100 mV, I_t = 2.3 nA, R_{gap}= 43.5 MΩ) showing both S- and Mo-layer structure presented by the bright and moderate contrast, respectively.

The intrinsic defects found in natural MoS_2 result in significant variation in the doping and contact resistance as demonstrated in our previous work.[34] Samples used in that study exhibited a large degree of variability across the *same* exfoliated MoS_2(0001) surface. For example, both n-type and p-type conductivities have been detected across the same natural MoS_2 surface, and the stoichiometry, as determined from the surface S/Mo atomic concentration ratio, can vary from 1.8 to 2.3. The variation in the electronic properties was correlated to two different types of defects: metal-like and structural. The presence of intrinsic metallic-like defects on the MoS_2 surface results in a parallel conduction path, which can explain the low electron Schottky barrier (metal/MoS_2) that is observed even in contact with high work function metals.[8,34−36] To achieve a low resistance contact, the electronic, chemical, and physical properties at the interface need to be carefully controlled. An earlier report identified the unexpected low Schottky barrier height for metal/MoS_2 contacts and attributed this to Fermi level pinning. However, the details of the interface chemistry and presence of defect-induced parallel conduction paths were not considered in that work.[36]

The introduction of well-controlled defects is a potential route for tuning new functionalities, such as those under consideration for graphene and graphene-related materials.[37−39] A recent report on elemental analysis of geological MoS_2 highlighted the role of defects on doping and contact resistance.[40] The purpose of this study is to outline the diverse intrinsic defects detected on exfoliated natural MoS_2. We characterize and compare the MoS_2 samples from the two main sources of molybdenite located in Australia ("a-MoS_2") and Canada ("c-MoS_2") that have been commonly utilized for exfoliation and device studies. Understanding the role of such structural and/or metallic imperfections on the top-surface/subsurface of the MoS_2 crystals is crucial for establishing what happens in or at the vicinity of the interface of an integrated device where the TMD surface could be in contact with a dielectric or a metal. The comprehension of those defects is illustrated and interpreted in this detailed study.

RESULTS AND DISCUSSION

Variability of the Defect Areal Density and Atomic Structure. The first type of noticeable defects on the exfoliated MoS_2 crystal surface is the presence of dark concave (pit) regions detectable in STM images larger than 200 × 200 nm^2. The areal density of such defects varies across a relatively small surface area (0.01 μm^2) of the same surface. The largest areal defect density is estimated to be about 10% with an average roughness of ∼1 nm as shown in Figure 1a, and the smallest areal density, with only a few detectable defects, is estimated to be less than 1.5%, as presented in Figure 1b. The surface in this region exhibits an average roughness of about 0.5 nm: 2 times less than the high defect density region presented in Figure 1a. Figure 1c presents a line profile measured on the surface in Figure 1b across a dark defect and indicates that the width of the defect is about 5 nm. The height is measured at about 0.6 nm, corresponding to the value of $c/2$ (0.616 nm) in bulk MoS_2.[12] It has been reported that the depth of the dark defects varies with the applied positive bias voltage (V_{bias});[31,41] the higher bias corresponds to the shallower depth, thus explaining the depth values changing between 0.3 and 0.7 nm. Dark defects generally have a circular shape with a diameter varying between 3 and 5 nm.

Imaging a defect-free region requires a high magnification of a small area to avoid the presence of defects. Figure 1d shows an example of the atomic structure recorded on a MoS_2(0001) surface showing the expected hexagonal pattern having a unit cell, a, of 0.34 ± 0.03 nm, similar to that found in previous investigations[13,17,31] and identical to the bulk model structure indicated in Figure 1e.[12] The structure is consistent with the semiconducting phase 2H-MoS_2; in contrast, the metallic distorted 1T′ phase was not detected.[42] The root-mean-square (rms) roughness (z_{rms}) measured on the defect-free area is very

low (z_{rms} = 0.14 ± 0.04) nm. The topmost sulfur layer causes the bright contrast forming the hexagonal structure, while the image of the underlying Mo-layer is taken under different imaging conditions. For example, the STM image shown in Figure 1f is recorded at V_b = 100 mV and a tunneling current, I_t, *of* 2.3 nA is measured showing two levels of contrast corresponding to the two topmost layers (S- and Mo-layer). In contrast, the STM image showing just the topmost S-layer in Figure 1d is recorded at V_b = 150 mV and I_t = 0.2 nA. The high resolution STM images are recorded with a relatively low effective gap resistance (R_{gap} < 100 MΩ), as presented by the well-resolved STM image in Figure 1f.

Morphological Defects. The surface morphology of MoS_2 exhibits several types of structural defects (Figure 2). The topography of the area shown in Figure 2a appears highly corrugated in comparison to the STM images in Figure 1, with a roughness >2 nm. This causes difficulties in identifying the atomic structure and acquiring images in negative bias, which may be due to the electron depletion that causes local band-bending.[31,41] Scanning tunneling spectroscopic analysis at room temperature also shows a peculiar electronic nature in specific regions, and this observation is discussed further in the STS section. Occasionally, large pits are also detected with a few nanometers in depth as shown in Figure 2b. In the case of Figure 2b the pit is 3 nm in depth and is equivalent to five layers of MoS_2 (Figure 2c), showing several step edges on the same region. This large pit could be a result of the aggressive nature of the mechanical exfoliation, which could also be responsible for other structural defects. We also observed a large structural defect, which appears to be associated with a large void underneath the top surface (Supporting Information Figure S1). The measured depth is less than 0.3 nm, and the MoS_2 atomic structure remains the same on and around the defect.

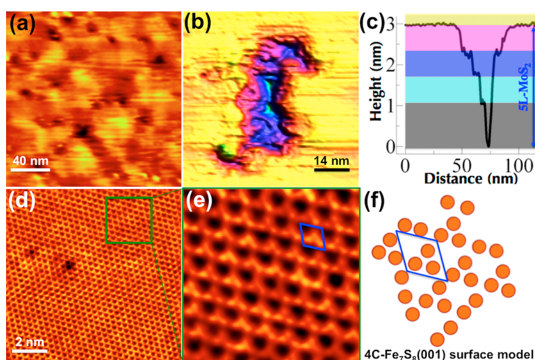

Figure 2. Additional structural defects observed on c-MoS_2. (a) STM image (V_{bias} = +1 V, I_t = 1 nA) shows a highly corrugated area. (b) STM image (V_{bias} = +1.1 V, I_t = 0.7 nA) shows a giant pit. (c) Line profile across the pit presented in panel b. (d) STM image (V_b = +200 mV, I_t = 3 nA) presents an unexpected superstructure; the depression corresponds to a single vacancy. This phase was only observed on a c-MoS_2 sample. (e) Enlargement (2.5 nm × 2.5 nm) of an area from STM image in panel d describing the atomic structure of the new pattern. (f) Structural model of topmost S-layer in the 4C-Fe_7S_8 (001) plan (ref 43) illustrating the atomic structure of the new phase observed on MoS_2.

One of the unexpected and new defect structures measured by STM at room temperature is described in Figure 2d−f. By carefully analyzing the high resolution STM image in Figure 2e obtained from the outlined area in Figure 2d, we identified a structure with a triangular shape. This is similar to the atomic structure of the monoclinic pyrrhotite 4C-Fe_7S_8(001) surface, as depicted by the structural model in Figure 2f.[43] The model shows only the topmost sulfur layer in the Fe_7S_8(001) surface. The fast Fourier transform (FFT) reveals additional spots around the center in comparison to the FFT calculated from the pristine MoS_2(0001) surface, confirming an alternative reconstruction (Supporting Information Figure S2). The unit cell, as outlined in Figure 2e, is measured to be about 0.35 nm, similar to the unit cell of the 2H-MoS_2 phase. The photoemission analysis shows the detection of only two states Mo^{4+} and S^{2-} confirming the chemical states of the MoS_2. We speculate that this phase is a local surface reconstruction.

Defects Characteristics. In addition to the variation in the density of defects across the surface of the MoS_2 crystals, the bias dependent test also shows varying behavior for the dark concave defects for both MoS_2 crystal sources (Figure 3 and Supporting Information Figure S3). By comparing the same area outlined in Figure 3a,b, under opposite biasing conditions, we observe that one of the dark defects in positive bias (Figure 3a) appears bright under negative bias conditions (white and black circles in Figure 3b). Previous studies[31,41,44] reported similar defect behavior on an ion-irradiated MoS_2 surface. The bright defects are attributed to Mo-like defects caused by the missing topmost S layer, and the dark defects as a missing layer segment (S−Mo−S) within or beneath the topmost layer. However, in this study, the MoS_2 crystals were not irradiated. Samples were simply exfoliated and loaded to ultrahigh vacuum without any other treatment or surface preparation.

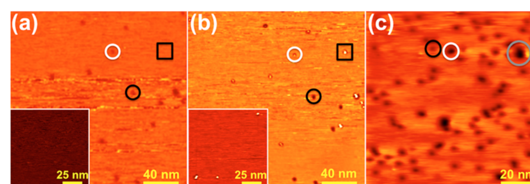

Figure 3. STM images recorded on a-MoS_2 sample. (a) STM image (V_{bias} = 1.15 V, I_t = 0.5 nA). (b) STM image (V_{bias} = −1.15 V, I_t = 0.5 nA) imaged on the same area as panel a. Inset for panel a: STM image (V_{bias} = +1.15 V, I_t = 0.8 nA) appears as if it were a defect-free area. Inset for panel b: STM image (V_{bias} = −1.15 V, I_t= 0.8 nA), recorded at the same area as the inset in panel a, shows the appearance of bright defects. (c) STM image (V_{bias} = +0.4 V, I_t = 1 nA) shows high defect density. The dark defects possess three different depths 0.6, 1.3, and 2.1 nm outlined by black, white, and gray circles, respectively. Line profiles across the outlined defects in panel c are presented in Supporting Information Figure S4.

The presence of structural defects on the as-exfoliated surface has only occasionally been reported,[32,45,46] with other reports implying that the surface is largely "defect-free".[5,13,14,42] At the atomic scale examined here, it is clear that a significant density of surface defects can be detected over areas equivalent to future device dimensions and that such defects may affect the behavior of contacts, dielectrics, and channel performance of exfoliated MoS_2. The dark regions bordering the bright defects were previously explained by local band-bending generated by Coulomb repulsion.[31,41] In addition, these STM images indicate a different defect behavior as outlined by the black square in Figure 3a,b, where a bright defect at negative bias disappears at positive bias. Moreover, the STM image measured at positive biases (inset to Figure 3a) shows a very flat surface with an average roughness of <0.35 nm without any indication

DOI: 10.1021/acsami.5b01778
ACS Appl. Mater. Interfaces 2015, 7, 11921−11929

of structural defects or imperfections. Nevertheless, the imaging performed at negative biases (inset to Figure 3b) indicates the presence of bright defects with a height measured between 0.3 and 0.6 nm (the height is strongly dependent on the imaging parameters V_{bias} and I_t). This demonstrates that a new defect type is detected on this unintentionally doped surface, which is similar to that detected on cleaved Re-doped synthetic $MoSe_2$(0001).[28] The Re atom possesses one more electron in comparison to Mo atom; substituting a Mo by a Re atom will n-type dope the MoS_2 sample. At negative bias, the filled states at the Fermi level are dominated by the partial density of states (DOS) of Re. At positive bias, the S density of state dominates the local DOS.

Figure 3c shows a MoS_2 surface region with a large defect density, where the areal density of imperfections is estimated at about 7% thus inducing an rms roughness of about 1.75 nm. Interestingly, the dark defects have three depths: 0.6 ± 0.1 nm, 1.3 ± 0.3 nm, and 2.1 ± 0.2 nm (Figure 3c), which correspond in the bulk structure to $^1/_2 \times c$, $1 \times c$, and $^3/_2 \times c$, respectively (Supporting Information Figure S4). In contrast, the c-MoS_2 investigated here exhibits only one depth corresponding to $^1/_2 \times c$ (Supporting Information Figure S3). These results indicate that exfoliated MoS_2 has substantial variability at the atomic scale. The STM image is similar to the MoS_2 surface morphology after submonolayer metal exposure. The measured atomic structure of the a-MoS_2 surface, which is identical to the previous structure (in Figure 1d), shows a hexagonal pattern with expected unit cell of (0.33 ± 0.03) nm and is consistent with that of the 2H polytype. The average roughness measured on defect-free area is around 0.1 nm. The areal density of the bright defects is estimated to be 0.2−0.8 atomic %, approaching the chemical detection limit of techniques such as XPS. It is worth noting that reduction of the sample thickness from millimeter to few nanometers does not change the defect characteristics (nature, size, density, and electronic structure), as recently reported.[46]

Other types of defects are also observed on the MoS_2 surfaces as shown in Figure 4. Figure 4a shows an STM image acquired at negative bias with several bright defects with and without the dark region surrounding the defect. The dark area surrounding the defect is not generated by a difference in the height but by electron deficiency caused by the local band-bending induced by the Coulomb repulsion (otherwise impurities or metallic-like defects).[31,41] The difference in the dark (depletion) region present around the defects in Figure 4a could be a result of a specific impurity or local structure. The tip−surface interaction can be excluded since the same tunneling current and the bias are used to collect the STM image for both types of defects. We argue that the electron depletion caused by the Coulomb repulsion is occurring around negatively ionized S atoms or impurities. Such a depletion area is recorded as a dark region by the metallic tip owing to the local band-bending or screening length.[41]

The bright defects shown in Figure 4 have different shapes: (i) cluster-like in Figure 4b, (ii) depression in the center of the cluster in Figure 4c, (iii) structured clusters in Figure 4d, and (iv) ring-structured defects in Figure 4e. The ring-structure defects surrounded by dark areas are similar to that reported for the MoS_2 surface after Na adsorption[47] which may suggest the presence of impurities (below the XPS detection limit) on the surface or intercalated within these crystals. Figure 4f shows yet another type of bright defect; indeed, the morphological behavior of this bright defect is totally different from the metallic-like defects. Similar imperfections are identified in other transition metal dichalcogenides such as $MoSe_2$ and WSe_2.[20,28,48] Such nanometer-scale bright spots have been attributed to trapped electron states around a donor on the surface chalcogen-atom layer.[16,20]

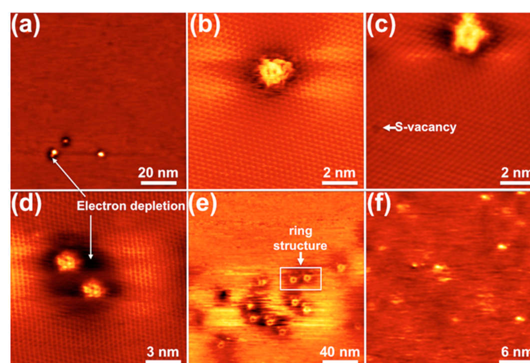

Figure 4. Additional defects observed on the exfoliated geological c-MoS_2. (a) STM image (V_{bias} = −300 mV, I_t = 0.5 nA) shows different dark regions around the bright defects; the dark regions are produced by the effect of electron depletion. (b) STM image (V_{bias} = −20 mV, I_t = 2 nA) indicating a bright defect appears as an amorphous cluster. (c) STM image (V_{bias} = −150 mV, I_t = 0.2 nA) shows a shaped bright defect with a depression in the center. (d) STM image (V_{bias} = −200 mV, I_t = 0.5 nA) shows two structured bright defects. (e) STM image (V_{bias} = −1 V, I_t = 0.7 nA) shows ring-structure imperfections. (f) STM image (V_{bias} = +50 mV, I_t = 1.3 nA) shows bright defects (or protrusions) similar to those once generated by alkali metals. Similar structures were observed on a-MoS_2 except for panels e and f.

The bright defects detected in the current study are similar in all aspects (bias dependence, shape, contrast, height) to the structures observed on 2H-MX_2 (M = Mo, W and X= S, Se) with impurities such as Li, Na, K, Rb, Cs, Re, I, and Cl at atomic concentrations[16,28,32] (e.g., Re-doped $MoSe_2$ <0.05%[28]). The XPS measurements performed on all geological MoS_2 bulk crystals studied here do not show any detectable impurities other than oxygen and carbon (Supporting Information Figure S5). Moreover, as noted previously, the topography of both exfoliated MoS_2 surfaces investigated is dominated by the dark/bright defects that were not intentionally created by Ar^+/He^+ ion bombardment as previously reported.[31,41]

Point Defects: Vacancies and Impurities. The surface of both a-MoS_2 and c-MoS_2 crystals frequently exhibits local intensity variations in STM images. Figure 5 shows examples of dark and bright imperfections with sizes ranging from a few angstroms to a few nanometers. The local change in the contrast observed in Figure 5a as a local depression and in Figure 5b as a bright location could be explained by the presence of impurities below the XPS detection limit, but could be detected by more sensitive methods such as inductively coupled plasma mass spectrometry discussed in more detail below. The local depression of 0.03 nm is not considered a vacancy since a missing S atom would result in a depth of ∼0.2 nm. The unit cell is fully preserved, and such defects do not disturb the surrounding lattice geometry. However, an impurity located at or around the S atom site could produce the depression (acceptor atom).[49] Such a depression could also be induced by a vacancy located at the subsurface layer.[50] Likewise, the bright contrast observed in Figure 5b could be caused by impurities located beneath or atop the topmost surface (donor atom).[49] Topographically, the local contrast changes the overall rms roughness slightly by an amount 0.02−0.05 nm.

DOI: 10.1021/acsami.5b01778
ACS Appl. Mater. Interfaces 2015, 7, 11921−11929

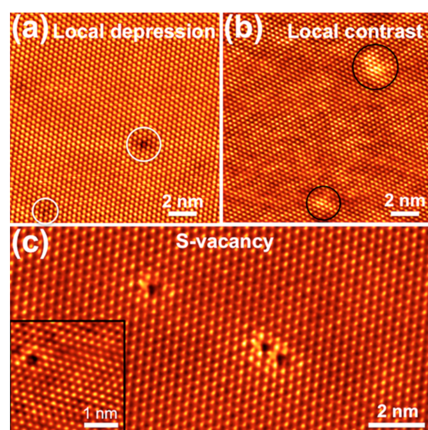

Figure 5. Survey of atomic imperfections observed on as-exfoliated a-MoS_2. (a) STM image (V_{bias} = +150 mV, I_t = 1.5 nA) presents several local depressions as outlined by a circle. (b) STM image (V_{bias} = 0.55 V, I_t = 1.5 nA) shows locally a high contrast observed on very flat surface, with the most clear examples outlined. (c) STM image (V_{bias} = −150 mV, I_t = 1.5 nA) shows three vacancies with high contrast at the vicinity of the point defect. Inset to panel c: STM image (5 nm × 5 nm, V_b = +150 mV, I_t = 0.2 nA) shows a single vacancy on c-MoS_2.

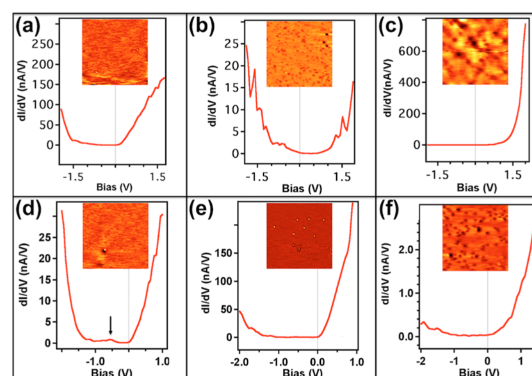

Figure 6. Differential conductance curves measured at room temperature on natural MoS_2. On c-MoS_2 sample: (a) n-type behavior, (b) p-type behavior, (c) spectrum showing a flat valence band with Fermi level shifted from conduction band minimum. On a-MoS_2: (d) n-type behavior with a defect feature (arrow) in the band gap, (e) n-type STS on an area less defective than that shown in panel f, (f) n-type behavior with very low conductivity at negative bias. The inset of each dI/dV curve corresponds to the STM image (100 nm × 100 nm) illustrating the typical topography where the $I(V)$ curves were carried out.

Regarding the vacancy defect, no obvious difference is noted between the sources of MoS_2. Identical single vacancies are observed on c-MoS_2 and on a-MoS_2 (Figure 5c).

The contrast in the vicinity of the vacancy is more notable than that in defect-free regions, which explains the change in the local density of states caused by the missing S atom as demonstrated by *ab initio* calculations.[33] The tunneling current is sensitive to the partial electron density associated with the surface Fermi level. Such a situation is easily created when the surface structure has a single atomic vacancy. Adjacent vacancies are also observed as shown in Figure 5c where the separation between the two vacancies is measured at ~0.63 nm corresponding to two unit cells. The depth of the vacancy is measured at 0.19 nm in agreement with the distance between S−Mo layers along the *z*-direction (Figure 1e). An acceptor atom located at a subsurface region can also cause the depression.[49] The bright contrasts may also be caused by the accumulation of negative charge induced by a donor atom. The difference between the intensity in the outlined area in panels a and b of Figure 5 is correlated with dopant localization in two different subsurface layers.[49,50] Similar observations were generated by defects in AsGa, InP, GaP, and InSb semiconductor surfaces.[49]

MoS_2 Electronic Structure: Scanning Tunneling Spectroscopy Studies. In this section, STS measurements were employed to identify the electronic characteristics of the MoS_2 crystals from both sources. The spectra are presented in terms of tunneling conductance (dI/dV) versus sample bias. The first derivative dI/dV, calculated from the current−voltage I−V, is proportional to the local electron density of states (LDOS) of the surface and permits one to determine the conduction and valence band edges that define the band gap.[51,52]

The dI/dV spectra show large variability over the exfoliated MoS_2 surface. Three typical characteristics of the spectra are identified: (a) n-type conductivity (Fermi level E_F near the conduction band (CB) edge), (b) p-type conductivity (E_F near the valence band (VB) edge), and (c) a flat valence band (dI/dV = 0, at negative bias). The n-type spectrum indicated in Figure 6a is identified on a surface with a near zero defect density. The band gap is measured to be 1.3 ± 0.1 eV, consistent with the values reported in previous studies.[46,53,54] The STS shown in Figure 6b exhibits a p-type behavior found on areas with apparent structural defects exhibiting a high defect density, with the corresponding STM image shown in the inset of Figure 6b. The band gap variation observed on or in the vicinity of the p-type/defective regions could be explained by local stress created by either S-rich/Mo-deficiencies or impurities.

One of the dominant electronic signatures measured on a rough region is illustrated in Figure 6c, where dI/dV is equal to zero at a negative bias. This behavior has previously been assigned to the local tip-induced band-bending effect (TIBB) as observed on WSe_2.[21] In conventional semiconductors, the TIBB phenomenon is a source of error in the STS analysis and band gap measurements.[55,56] The TIBB effect occurs in the metal−insulator−semiconductor (MIS) junction presented here due to the (tungsten tip)/(vacuum gap)/MoS_2 structure associated with the measurement technique. The band-bending prevents electron tunneling from the valence band of the semiconducting substrate to the metallic W tip. Using the same tip across the single MoS_2 surface and the same imaging conditions (applied bias V_{bias}, and tunneling current I_t), the observed zero-conductance is observed on several spots independent of the tip−surface distance or the tip shape, suggesting that the effect is not tip-induced. Instead, we note that measuring a zero tunneling current while probing filled states could be induced by band-bending due to surface defects or a charge trapping mechanism (instead of TIBB).[58,59] This unbalanced state causes local changes in the conductivity behavior and the band gap. This is an expected effect due to local variations in the nature and the concentration of the imperfections. To sum up, it is clear from Figure 6c that the highly defective surface changes the STS spectrum in two ways: (i) Fermi level shift of 1 V away from the conduction band and (ii) dI/dV = 0 at negative bias.

Spectroscopic measurements also show another electronic signature with n-type STS behavior suggesting the presence of a feature in the band gap located 0.65 eV below the Fermi level

DOI: 10.1021/acsami.5b01778
ACS Appl. Mater. Interfaces 2015, 7, 11921−11929

Table 1. Comparison of ICPMS Data Collected on Both MoS_2 Sources[a]

	abundance (ppb)										
	Al	Ca	Cu	Fe	Mg	Mn	P	Na	Ti	W	Zn
a-MoS_2	52.6	5.7	21.3	44.3	2.32	2.31	10.5	18.7	1.4	6.68	7.8
c-MoS_2	9.6	<1.0	<1.0	37.4	<1.0	<1.0	5.0	2.82	2.17	1.84	<1.0

[a]The abundance unit is parts-by-billion by weight.

(Figure 6d and Supporting Information Figure S6). A comparable feature[46] was also observed above the valence band maximum in the calculated density of states on the MoS_2 monolayer with induced defects.[33,57]

The n-type regions shown in Figure 6e,f suggest that there is a variation in the surface defect density: the low defect density (inset to Figure 6e) and high defect density regions (inset Figure 6f) exhibit low conductivity at negative bias which could be caused by TIBB, electron depletion, and/or the surface defect-induced band-bending. The band gap is estimated at ~1.25 eV with the conduction band minimum reproducibly located at 0 eV, consistent with prior reports of bulk MoS_2. The high current measured at negative bias on the area shown in Figure 6e could be caused by the Mo-like defects on the surface as reported previously.[34] We conclude from the STS observations that impurities or other defects located at the surface/subsurface cause local electron depletion and band-bending resulting in a lowering and suppression of current from the occupied states. It is worth noting that the same band-bending behavior was also observed on semiconductor $TiO_2(110)$ and $TiO_2(011)$ phases induced by intrinsic and extrinsic defects.[58,59]

Impurity Detection. Recently, ICPMS was used to analyze MoS_2 minerals collected from 135 localities over the earth with known geological ages, and it was found that large amounts of transition elements such as Fe (~1000 ppm), W (~4000 ppm), and Re (5000 ppm), as well as high concentrations of Ni, Mn, Cu, Ru, Ca, and Co (>20 ppm, <1000 ppm), were found.[60] Re varies significantly depending on geological age and location of the MoS_2 on the earth. *Ab initio* calculations also reveal that Re behaves as a donor and alkali metals shift the Fermi level close to the conduction band edge making the MoS_2 n-type.[61]

We also used ICPMS, commonly utilized for quantitative impurity analysis in the semiconductor industry, to measure impurities in the samples used in this study.[62] While XPS has a detection limit of approximately 0.1%, ICPMS has a detection limit of better than 1 part-per-billion (ppb). Table 1 shows the concentration of elements measured at values higher than 1.0 ppb. In addition to Mo and S different impurities are present in amounts greater than 1.0 ppb: Al, Ca, Cu, Fe, Mg, Mn, P, Na, Ti, W, and Zn. These concentrations are consistent with previous secondary-ion mass spectroscopy (SIMS) evaluations that estimated the presence of several elements: Mn (0.5%), Al (0.4%) and Ca (1.5%).[63] Glow discharge mass spectrometry (GDMS) also indicated the presence of different types of impurities considered as intrinsic to MoS_2. In addition to the major impurities such as Ti (46 ppm) and V (19 ppm), GMDS reveals that F, Na, Al, Ca, K, Mn, Si, and Fe are present at concentrations less than 1 ppm.[64] Conversion of these levels to equivalent impurity concentrations in the MoS_2 host leads to the conclusion that impurities can easily exceed concentrations of $10^{10}/cm^2$, and would thus be expected to impact transport measurements if present as ionized impurities.[65,66]

The detection of such impurities in the bulk or near the surface of MoS_2 may explain the large variability found in the topography and the electronic structure of molybdenite samples. Nevertheless, substantial variations appear to be observed among the materials investigated, and comparisons to synthetic MoS_2 as well as other TMDs is underway.

DISCUSSION: CORRELATING THE OBSERVED VARIABILITY

Measurement of the MoS_2 surface is key to the understanding of interfaces and heterojunctions involving MoS_2. Since the majority of molybdenite used in device fabrication is currently provided from exfoliated geological sources, those same sources have been utilized in this work with complementary methods. After mechanical cleavage, annealing is performed in vacuum at 400 °C to desorb adventitious contamination (e.g., weakly bound organics detected as C and O surface impurities). The study of the $MoS_2(0001)$ surface using XPS and STM techniques before and after such annealing shows no detectable changes in the topography or the conductivity. High resolution STM images are obtained readily on as-exfoliated MoS_2 surface without any thermal treatment, and the hexagonal structure typically corresponds to the 2H semiconducting phase. These observations lead to the conclusion that carbon and/or oxygen species are not the origin of the p-type behavior observed on the expected n-type sample.

As XPS measurements indicate only C and O as detectable contaminant species, other impurities, if present, are below the detection limit of XPS. From STM/STS studies, a S-deficiency manifests itself as vacancies and pits on the pristine surface of MoS_2 caused by the missing atoms, thus potentially explaining the observed n-type conductivity. On the other hand, the S-rich surface is rough and corrugated, and we speculate that the high concentration of sulfur causes the structural defects and strain generating p-type conductivity and defect-induced zero conductivity behavior.[34] The p-type conductivity could of course be caused by the presence of impurities below the limit of XPS detection (e.g., Nb, Zr, Y).[61,67] STM images on the exfoliated MoS_2 crystal show a similar surface topography as that observed after alkali, Sn, or Re deposition.[28] As noted previously, some impurities, such as Re, are also expected to generate the n-type doping[60] and have been detected[61] in geological MoS_2 at concentrations anticipated to be significant for carrier scattering in device transport.[65]

To the best of our knowledge, this is the first report depicting the origin of the zero-conductance at negative bias (flat valence band) measured by room temperature STS on the highly defective MoS_2 surface. Intrinsic and extrinsic defects inducing band-bending were previously observed on different semiconducting surfaces such as $TiO_2(011)$.[59] This band-bending observed in MoS_2 shifts the Fermi level by about 1 eV from the conduction band edge. The variability in the surface defects and the impurities concentration variation between the two mineral sources explains the local areas of electron depletion. Such variations are also expected to impact device behavior variations reported in the literature.

DOI: 10.1021/acsami.5b01778
ACS Appl. Mater. Interfaces 2015, 7, 11921−11929

The single vacancy is assigned to the absence of a sulfur atom as predicted by *ab initio* calculations.[33] The S-vacancy creates a feature in the band gap region as measured by the STS and calculated by the density of states. *Ab initio* calculations[33,68] revealed that intrinsic defects (single vacancies, extended defects such as dislocations and grain boundaries) in MoS_2 can significantly impact the electron transport, even at very low concentration. The bright defects detected on a pristine surface are assigned to the cluster-like Mo formed from the absence of sulfur atoms. It has previously been explained that such defects provide a parallel conduction path with a low Schottky barrier than the regions with a direct high work function metal−MoS_2 interface.[34] The observed Schottky barrier measured is dominated by the lower of the two barriers, which means that even high work function metals can appear to have low Schottky barriers on n-type MoS_2 simply due to the presence of defects with concentrations as low as 0.3% lowering the Schottky barrier height as recently measured by $I-V$ characteristics and confirmed by simulation.[34] While XPS is a convenient *in situ* chemical analysis technique, the detection limit of the technique is insufficient to detect impurities that can have a significant impact on the electronic properties of TMD materials. Furthermore, the highly defective surface can be very reactive in air. The surface reactivity and perfection of MoS_2 or of any TMD material is a critical aspect that must be mitigated to enable high quality electronic devices.

■ CONCLUSION

In summary, we performed a detailed surface study of pristine natural $MoS_2(0001)$ surfaces after mechanical exfoliation, using room temperature scanning tunneling microscopy and spectroscopy, and X-ray photoelectron spectroscopy. Geological MoS_2 crystals obtained from Canada and Australia are typically consistent with 2H-MoS_2 atomic structures with structural and metallic-like defects at significant concentrations varying between 0.1% and 10%. The surfaces of MoS_2 from both sources display large local variation, expressed by the presence of both n- and p-type conductivities explained by sulfur-deficient or -rich regions. Point defects caused by sulfur vacancies are readily identified on both surfaces. The nanometer variation in the intensity of the STM images can also be explained by the presence of impurities as measured by ICPMS in the parts-per-billion level, but well below the limit of detection of XPS. Defects and impurities/dopants were found to induce the observed zero-conductance behavior at a negative bias as measured by STS. Finally, it is clear that the synthesis of high quality materials will be required before any TMD materials can be integrated into industrial scale processing. Of course, the absence of high quality synthetic crystals or thin films makes exploratory investigations of the electrical properties of these materials using geological sources a necessity. This study emphasizes that, for useful conclusions to be extracted from the electrical characterization of devices fabricated with geological MoS_2, a detailed understanding of the semiconductor material itself is required, and the impact of impurities and defects must be considered in the interpretation of device performance including carrier mobility.

■ MATERIALS AND METHODS

The geological MoS_2 specimens used in this study are purchased from two vendors: SPI and 2D Semiconductors.[69] The former provided molybdenite collected from Canada (c-MoS_2), and the latter provided MoS_2 mined from different sources including Australia (a-MoS_2). Crystals of $\sim 5 \times 5$ mm^2 and thickness larger than 0.2 mm were employed. The preparation of the crystal surface consists of mechanically cleaving (exfoliation) using transparent office tape. The crystals are then loaded within 1 min into an ultrahigh vacuum (UHV) chamber capable of achieving a base pressure in the low 10^{-10} mbar range. The UHV system (Supporting Information Figure S7) is a customized Omicron multiprobe-scanning probe microscope (SPM).[70] The SPM is a variable temperature design and allows analysis using traditional scanning tunneling microscopy (STM). The STM images and the scanning tunneling spectroscopy (STS) current−voltage dI/dV curves are acquired at room temperature in the constant-current mode using an etched tungsten tip. Imaging with a negative (positive) voltage examines the occupied (unoccupied) surface states. The dI/dV spectra are differentiated from an average of 10 $I(V)$ curves acquired sequential at a single location. Image processing of STM data are executed by *WSxM* software.

■ ASSOCIATED CONTENT

Supporting Information

Additional information including details of large structural defect, FFT comparison between 2H-MoS_2 and a new superstructure, bias dependence test, photoemission data, band gap defect in STS, and description of the UHV system used in this work. The Supporting Information is available free of charge on the ACS Publications website at DOI: 10.1021/acsami.5b01778.

■ AUTHOR INFORMATION

Corresponding Authors

*E-mail: addou@utdallas.edu.

*E-mail: rmwallace@utdallas.edu.

Notes

The authors declare no competing financial interest.

■ ACKNOWLEDGMENTS

The authors would like to thank Prof. Kyeongjae Cho, Prof. Julia W. P. Hsu, Prof. Christopher Hinkle, Dr. Stephen McDonnell, and Dr. Santosh KC for useful discussions. This work was supported in part by the Southwest Academy on Nanoelectronics (SWAN) sponsored by the Nanoelectronic Research Initiative (NRI).

■ REFERENCES

(1) Butler, S. Z.; Hollen, S. M.; Cao, L.; Cui, Y.; Gupta, J. A.; Gutiérrez, H. R.; Heinz, T. F.; Hong, S. S.; Huang, J.; Ismach, A. F.; Johnston-Halperin, E.; Kuno, M.; Plashnitsa, V. V.; Robinson, R. D.; Ruoff, R. S.; Salahuddin, S.; Shan, J.; Shi, L.; Spencer, M. G.; Terrones, M.; Windl, W.; Goldberger, J. E. Progress, Challenges, and Opportunities in Two-Dimensional Materials Beyond Graphene. *ACS Nano* **2013**, *7*, 2898−2926.

(2) Frindt, R. F. Single Crystals of MoS_2 Several Molecular Layers Thick. *J. Appl. Phys.* **1966**, *37*, 1928−1929.

(3) Lee, S.; Iyore, O. D.; Park, S.; Lee, Y. G.; Jandhyala, S.; Kang, C. G.; Mordi, G.; Kim, Y.; Quevedo-Lopez, M.; Quevedo-Lopez, M.; Gnade, B. E.; Wallace, R. M.; Lee, B. H.; Jim, J. Rigid Substrate Process to Achieve High Mobility in Graphene Field-Effect Transistors on a Flexible Substrate. *Carbon* **2014**, *68*, 791−797.

(4) Addou, R.; Dahal, A.; Sutter, P.; Batzill, M. Monolayer Graphene Growth on Ni(111) by Low Temperature Chemical Vapor Deposition. *Appl. Phys. Lett.* **2012**, *100*, 021601.

(5) Coy-Diaz, H.; Addou, R.; Batzill, M. Interface Properties of CVD Grown Graphene Transferred onto $MoS_2(0001)$. *Nanoscale* **2014**, *6*, 1071−1078.

(6) Geim, A. K.; Grigorieva, I. V. 2013 Van der Waals Heterostructures. *Nature* **2013**, *499*, 419−425.

DOI: 10.1021/acsami.5b01778
ACS Appl. Mater. Interfaces 2015, 7, 11921−11929

(7) Colombo, L.; Wallace, R. M.; Ruoff, R. S. Graphene Growth and Device Integration. *Proc. IEEE* **2013**, *101*, 1536−1556.
(8) Radisavljevic, B.; Radenovic, A.; Brivio, J.; Giacometti, V.; Kis, A. Single-Layer MoS_2 Transistors. *Nat. Nanotechnol.* **2011**, *6*, 147.
(9) Mak, K. F.; Lee, C.; Hone, J.; Shan, J.; Heinz, T. F. Atomically Thin MoS_2: A New Direct-Gap Semiconductor. *Phys. Rev. Lett.* **2010**, *105*, 136805.
(10) Pu, J.; Yomogida, Y.; Liu, K. K.; Li, L. J.; Iwasa, Y.; Takenobu, T. Highly Flexible MoS_2 Thin-Film Transistors With Ion Gel Dielectrics. *Nano Lett.* **2012**, *12*, 4013.
(11) El Beqqali, O.; Zorkani, I.; Rogemond, F.; Chermette, H.; Ben Chaabane, R.; Gamoudi, M.; Guillaud, G. Electrical Properties of Molybdenum Disulfide MoS_2 Experimental Study and Density Functional Calculation Results. *Synth. Met.* **1997**, *90*, 165.
(12) Dickinson, R. G.; Pauling, L. The Crystal Structure of Molybdenite. *J. Am. Chem. Soc.* **1923**, *45*, 1466.
(13) Stupian, G. W.; Leung, M. S. Imaging of MoS_2 by Scanning Tunneling Microscopy. *Appl. Phys. Lett.* **1987**, *51*, 1560.
(14) Youngquist, M. G.; Baldeschwieler, J. D. Observation of Negative Differential Resistance in Tunneling Spectroscopy of MoS_2 With a Scanning Tunneling Microscope. *J. Vac. Sci. Technol., B: Microelectron. Process. Phenom.* **1990**, *9*, 1083−1087.
(15) Magonov, S. N.; Whangbo, M. H. Interpreting STM and AFM Images. *Adv. Mater.* **1994**, *6*, 355−371.
(16) Magonov, S. N.; Whangbo, M. H. *Surface Analysis with STM and AFM: Experimental and Theoretical Aspects of Image Analysis*; VCH: Weinheim, 1996.
(17) Perrot, E.; Humbert, A.; Piednoir, A.; Chapon, C.; Henry, C. R. STM and TEM Studies of a Model catalyst: Pd/MoS_2(0001). *Surf. Sci.* **2000**, *445*, 407−419.
(18) Parkinson, B. A.; Ren, J.; Whangbo, M. H. Relationship of STM and AFM Images to the Local Density of States in the Valence and Conduction Bands of Rhenium Selenide ($ReSe_2$). *J. Am. Chem. Soc.* **1991**, *113*, 7833−7837.
(19) Kelty, S. P.; Ruppert, A. F.; Chianelli, R. R.; Ren, J.; Whangbo, M. H. Scanning Probe Microscopy Study of Layered Dichalcogenides ReS_2. *J. Am. Chem. Soc.* **1994**, *116*, 7857−7863.
(20) Magonov, S. N.; Cantow, H. J.; Whangbo, M. H. On the Nature of Nanometer-Scale Ring Structures in the Scanning Tunneling Microscopy Images of Tungsten Diselenide WSe_2. *Surf. Sci.* **1994**, *318*, 1175−1180.
(21) Yoshida, S.; Terada, Y.; Yokota, M.; Takeuchi, O.; Mera, Y.; Shigekawa, H. Direct Probing of Transient Photocurrent Dynamics in p-WSe_2 by Time-Resolved Scanning Tunneling Microscopy. *Appl. Phys. Express* **2013**, *6*, 016601.
(22) Cukjati, D.; Prodan, A.; Jug, N.; van Midden, H. J. P.; Starowicz, P.; Karic, E.; Hla, S. W.; Böhm, H.; Boswell, F. W.; Bennett, J. C. The Surface and Domain Structure of $NbTe_2$. *J. Cryst. Growth* **2002**, *237*−*239*, 278−282.
(23) Bengel, H.; Cantow, H. J.; Magonov, S. N.; Jung, D.; Ren, J.; Whangbo, M. H. Examination of the Corrugated Surfaces of $NbTe_2$ and WTe_2. *New J. Chem.* **1996**, *20*, 287−294.
(24) Tang, S. L.; Kasowski, R. V.; Parkinson, B. A. Scanning Tunneling of the Subsurface Structures of Tungsten Ditelluride and Molybdenum Ditelluride. *Phys. Rev. B* **1989**, *39*, 9987.
(25) Saidi, A.; Hasbach, A.; Raberg, W.; Wandelt, K. Atomic Force Microscopy and Scanning Tunneling Microscopy/Spectroscopy Investigations of Molybdenum Ditellurides. *J. Vac. Sci. Technol,. A* **1998**, *16*, 951.
(26) Hla, S. W.; Marinković, V.; Prodan, A.; Muševič, I. STM/AFM Investigations of β-$MoTe_2$, α-$MoTe_2$ and WTe_2. *Surf. Sci.* **1996**, *352*−*354*, 105−111.
(27) Chamlagain, B.; Li, Q.; Ghimire, N. J.; Chuang, H. J.; Perera, M. M.; Tu, H.; Xu, Y.; Pan, M.; Xaio, D.; Yan, J.; Mandrus, D.; Zhou, Z. Mobility Improvement and Temperature Dependence in $MoSe_2$ Field-Effect Transistors on Parylene-C Substrate. *ACS Nano* **2014**, *8*, 5079−5088.
(28) Murata, H.; Kataoka, K.; Koma, A. Scanning Tunneling Microscope Images of Locally Modulated Structures in Layered Materials, MoS_2(0001) and $MoSe_2$(0001), Induced by Impurity Atoms. *Surf. Sci.* **2001**, *478*, 131−144.
(29) Slough, C. G.; McNairy, W. W.; Coleman, R. V.; Drake, B.; Hansma, P. K. Charge-Density Waves Studied With the Use of a Scanning Tunneling Microscope. *Phys. Rev. B* **1986**, *34*, 994−1005.
(30) Coleman, R. V.; McNairy, W. W.; Slough, C. G.; Hansma, P. K.; Drake, B. Images of Charge-Density Waves Obtained With Scanning Tunneling Microscopy. *Surf. Sci.* **1987**, *181*, 112−118.
(31) Inoue, A.; Komori, T.; Shudo, K. I. Atomic-Scale Structures and Electronic States of Defects on Ar^+-Ion Irradiated MoS_2. *J. Electron Spectrosc. Relat. Phenom.* **2013**, *189*, 11−18.
(32) Whangbo, M. H.; Ren, J.; Magonov, S. N.; Bengel, H.; Parkinson, B. A.; Suna, A. On the Correlation Between the Scanning Tunneling Microscopy Image Imperfections and Point Defects of Layered Chalcogenides 2H-MX_2 (M=Mo, W; X= S, Se). *Surf. Sci.* **1995**, *326*, 311−326.
(33) KC, S.; Longo, R. C.; Addou, R.; Wallace, R. M.; Cho, K. Impact of Intrinsic Atomic Defects on the Electronic Structure of MoS_2 Monolayers. *Nanotechnology* **2014**, *25*, 375703.
(34) McDonnell, S.; Addou, R.; Buie, C.; Wallace, R. M.; Hinkle, C. L. Defect-Dominated Doping and Contact Resistance in MoS_2. *ACS Nano* **2014**, *8*, 2880−2888. The "c-MoS_2" was utilized in this study.
(35) Liu, H.; Neal, A. T.; Ye, P. D. Channel Length Scaling of MoS_2 MOSFETs. *ACS Nano* **2012**, *6*, 8563−8569.
(36) Das, S.; Chen, H. Y.; Penumatcha, A. V.; Appenzeller, J. High Performance Multi-Layer MoS_2 Transistors With Scandium Contacts. *Nano Lett.* **2013**, *12*, 100−105.
(37) Araujo, P. T.; Terrones, M.; Dresselhaus, M. S. Defects and Impurities in Graphene-Like Materials. *Mater. Today* **2012**, *15*, 98−109.
(38) Lahiri, J.; Lin, Y.; Bozkurt, P.; Oleynik, I. I.; Batzill, M. An Extended Defect in Graphene as a Metallic Wire. *Nat. Nanotechnol.* **2010**, *5*, 326−329.
(39) Terrones, H.; Ruitao, Lv.; Terrones, M.; Dresselhaus, M. S. The Role of Defects and Doping in 2D Graphene Sheets and 1D Nanoribbons. *Rep. Prog. Phys.* **2012**, *75*, 062501.
(40) Sreeprasad, T. S.; Nguyen, P.; Kim, N.; Berry, V. Controlled, Defect-Guided, Metal-Nanoparticle Incorporation Onto MoS_2 Via Chemical and Microwave Routes: Electrical, Thermal, and Structural Properties. *Nano Lett.* **2013**, *13*, 4434−4441.
(41) Sengoku, N.; Ogawa, K. Investigations of Electronic Structures of Defects Introduced by Ar Ion Bombardments on MoS_2 by Scanning Tunneling Microscopy. *Jpn. J. Appl. Phys.* **1995**, *34*, 3363−3367.
(42) Wypych, F.; Weber, T.; Prins, R. Scanning Tunneling Microscopic Investigation of 1T-MoS_2. *Chem. Mater.* **1998**, *10*, 723−727.
(43) Becker, U.; Munz, A. W.; Lennie, A. R.; Thornton, G.; Vaughan, D. J. The Atomic and Electronic Structure of the (001) Surface of Monoclinic Pyrrhotite (Fe_7S_8) as Studied Using STM, LEED and Quantum Mechanical Calculations. *Surf. Sci.* **1997**, *389*, 66−87.
(44) Park, J. B.; France, C. B.; Parkinson, B. A. Scanning Tunneling Microscopy Investigation of Nanostructures Produced by Ar^+ and He^+ Bombardment of MoS_2 Surfaces. *J. Vac. Sci. Technol., B: Microelectron. Nanometer Struct.—Process., Meas., Phenom.* **2005**, *23*, 1532.
(45) Hosoki, S.; Hosoka, S.; Hasegawa, T. Surface Modification of MoS_2 Using an STM. *Appl. Surf. Sci.* **1992**, *60*, 643−647.
(46) Lu, C.-P.; Li, G.; Mao, J.; Wang, L.-M.; Andrei, E. Y. Bandgap, Mid-Gap States, and Gating Effects in MoS_2. *Nano Lett.* **2014**, *14*, 4628−4633.
(47) Abe, H.; Kataoka, K.; Ueno, K.; Koma, A. Scanning Tunneling Microscope Observation of the Metal-Adsorbed Layered Semiconductor Surfaces. *Jpn. J. Appl. Phys.* **1995**, *34*, 3343−3345.
(48) McDonnell, S.; Azcatl, A.; Addou, R.; Gong, C.; Battaglia, C.; Chuang, S.; Cho, K.; Javey, A.; Wallace, R. M. Hole Contacts on Transition Metal Dichalcogenides: Interface Chemistry and Band Alignments. *ACS Nano* **2014**, *8*, 6265−6272.
(49) Ebert, Ph. Nano-Scale Properties of Defects in Compound Semiconductor Surfaces. *Surf. Sci.* **1999**, *33*, 121−303.

DOI: 10.1021/acsami.5b01778
ACS Appl. Mater. Interfaces 2015, 7, 11921−11929

(50) Matthes, Th. W.; Sommerhalter, Ch.; Rettenberger, A.; Bruker, P.; Boneberg, J.; Lux-Steiner, M. Ch.; Leiderer, P. Imaging of Dopants in Surface and Sub-Surface Layers of the Transition Metal Dichalcogenides WS_2 and WSe_2 by Scanning Tunneling Microscopy. *Appl. Phys. A: Mater. Sci. Process.* **1998**, *66*, S1007−S1011.
(51) Stroscio, J. A.; Feenstra, R. M.; Fein, A. P. Electronic Structure of the Si(111)2 × 1 Surface by Scanning Tunneling Microscopy. *Phys. Rev. Lett.* **1986**, *57*, 2579.
(52) The normalized differential conductance dI/dV by the total conductance I/V provides the surface DOS. The $(dI/dV)/(I/V)$ plot highlights the relevant DOS features independently of the tip−sample distance, and the exponential divergence in the applied voltage.
(53) Kautek, W.; Gerischer, H.; Tributsch, H. The Role of Carrier Diffusion and Indirect Optical Transitions in the Photoelectrochemical Behavior of Layer Type D-Band Semiconductors. *J. Electrochem. Soc.* **1980**, *127*, 2471−2478.
(54) McDonnell, S.; Brennan, B.; Azcatl, A.; Lu, N.; Dong, H.; Buie, C.; Kim, J.; Hinkle, C. L.; Kim, M. J.; Wallace, R. M. HfO_2 on MoS_2 by Atomic Layer Deposition: Adsorption Mechanisms and Thickness Scalability. *ACS Nano* **2013**, *7*, 10354−10361.
(55) Narita, H.; Kimura, A.; Taniguchi, M.; Nakatake, M.; Xie, T.; Qiao, S.; Namatame, H.; Yang, S.; Zhang, L.; Wang, E. G. Tip-Induced Band Bending Effect and Local Electronic Structure of Al Nanoclusters on Si(111). *Phys. Rev. B* **2008**, *78*, 115309.
(56) Dombrowski, R.; Steinebach, C.; Wittneven, C.; Morgenstern, M.; Wiesendanger, R. Tip-Induced Band Bending by Scanning Tunneling Spectroscopy of the States of the Tip-Induced Quantum Dot on InAs(110). *Phys. Rev. B* **1999**, *59*, 8043.
(57) Fuhr, J. D.; Saúl, A. G.; Sofo, J. O. STM Chemical Signature of Point Defects on the MoS_2(0001) Surface. *Phys. Rev. Lett.* **2004**, *92*, 026802.
(58) Batzill, M.; Katsiev, K.; Gaspar, D. J.; Diebold, U. Variations of the Local Electronic Surface Properties of TiO_2(110) Induced by Intrinsic and Extrinsic Defects. *Phys. Rev. B* **2002**, *66*, 235401.
(59) Tao, J.; Luttrell, T.; Batzill, M. A Two-Dimensional Phase of TiO_2 With a Reduced Bandgap. *Nat. Chem.* **2011**, *3*, 296−300.
(60) Golden, J.; McMillan, M.; Downs, R. T.; Hystad, G.; Goldstein, I.; Stein, H. J.; Zimmerman, A.; Sverjensky, D. A.; Armstrong, J. T.; Hazen, R. M. Rhenium Variations in Molybdenite (MoS_2): Evidence for Progressive Subsurface Oxidation. *Earth Planet. Sci. Lett.* **2013**, *366*, 1−5.
(61) Dolui, K.; Rungger, I.; Das Pemmarajau, C.; Sanvito, S. Possible Doping Strategies for MoS_2 Monolayers: An *Ab Initio* Study. *Phys. Rev. B* **2013**, *88*, 075420.
(62) Beauchemin, D. Inductively Coupled Plasma Mass Spectrometry. *Anal. Chem.* **2006**, *78*, 4111−4136.
(63) Heckl, W. M.; Ohnesorge, F.; Binnig, G. Ring Structures on Natural Molybdenum Disulfide Investigated by Scanning Tunneling and Scanning Force Microscopy. *J. Vac. Sci. Technol., B: Microelectron. Nanometer Struct.—Process., Meas., Phenom.* **1991**, *9*, 1072−1078.
(64) Ha, J. S.; Roh, H. S.; Park, S. J.; Yi, J. Y.; Lee, E. H. Scanning Tunneling Microscopy Investigation of the Surface Structures of Natural MoS_2. *Surf. Sci.* **1994**, *315*, 62−68.
(65) Ma, N.; Jena, D. Charge Scattering and Mobility in Atomically Thin Semiconductors. *Phys. Rev. X* **2014**, *4*, 011043.
(66) Sze, S. M.; Ng, K. K. *Physics of Semiconductor Devices*; Wiley: New York, 2007.
(67) Suh, J.; Park, T. E.; Lin, D. Y.; Fu, D.; Park, J.; Jung, H. J.; Chen, Y.; Ko, C.; Jang, C.; Sun, Y.; Sinclair, R.; Chang, J.; Tongay, S.; Wu, J. Doping Against the Native Propensity of MoS_2: Degenerate Hole Doping by Cation Substitution. *Nano Lett.* **2014**, *14*, 6976−6982.
(68) Ghorbani-Asl, M.; Enyashin, A. N.; Kuc, A.; Seifert, G.; Heine, T. Defect-Induced Conductivity Anisotropy in MoS_2 Monolayers. *Phys. Rev. B* **2013**, *88*, 245440.
(69) c-MoS_2 crystals are purchased from SPI vendor, http://www.2spi.com/, and a-MoS_2 from 2D semiconductors vendor, http://www.2dsemiconductors.com/.
(70) Wallace, R. M. In-Situ Studies on 2D Materials. *ECS Trans.* **2014**, *64*, 109−116.